Design and Characterization of Phase Holograms for Standoff Localization at Millimeter and Submillimeter Waves

Samu-Ville Pälli, Aleksi Tamminen, *Member, IEEE*, Juha Ala-Laurinaho, and Zachary D. Taylor, *Member, IEEE*

***Abstract*— We present design, simulation, and experimental characterization of dual-band frequency-diverse holograms for distributed beamforming. The holograms operate in the 50–75 GHz (WR-15) and 220–330 GHz (WR-3.4) bands for millimeter- and submillimeter-wave imaging. The holograms are designed to create a dispersive field in the region of interest (RoI) located 600 mm from the aperture. The holograms lie in the front end of an imaging setup and modulate the phase of the incident collimated beam from a parabolic mirror. The distributed beamforming enables interrogation of the RoI so that the measured reflection through the dispersive propagation path conveys the spatial information of the target. Different phase modulation schemes are evaluated, and two prototype holograms are manufactured. The dispersive operation and efficiency of the hologram are characterized with both simulations and measurements. The frequency diversity of the holograms is quantified using singular-value decomposition and spatial-spectral correlation coefficient methods. The results identified a design frequency of 120 GHz, a phase quantization step of $\pi/2$ radians, and an added phase of 1.9π radians as a good dispersion-efficiency compromise. A fully connected neural network is trained to localize a corner-cube reflector in the RoI illuminated by the hologram. The localization accuracy follows the diffraction-limited resolution and confirms the best performance for the hologram considered optimal in the design metrics.**

***Index Terms*— Beamforming, hologram, localization, millimeter waves (mm-waves), submillimeter waves.**

I. Introduction

BEAMFORMING is a key capability in millimeter-wave (mm-wave) and submillimeter-wave imaging with active applications research in areas, including medical sensing, nondestructive testing, and personnel screening. The nonionizing nature and the ability to penetrate various materials, while maintaining sufficient imaging resolution, illustrate the potential of millimeter- and submillimeter-wave technologies. Many applications under research require real-time imaging, necessitating fast beamsteering capability. Typically, the 10-Hz frame rate is considered to approximate real time in the applications where moving human subjects are to be imaged.

Conventional imaging methods at mm-waves are often based on raster scanning the beam in the region of interest (RoI) mechanically or electronically [1], [2]. In mechanical scanning, the object plane focal point is steered by mirrors actuated by high-accuracy mechanical drives. In electronic scanning, the beam is manipulated by an array of phase- or amplitude-shifting elements. However, mechanical solutions involve wearing parts requiring maintenance and can have a large footprint. Electronic beamsteering systems are typically arrays with, e.g., thousands of phase-coherent sensors. Sensor count is associated with rapidly increasing cost and complexity, especially in the submillimeter-wave regime. In real-time imaging scenarios, the applicability of these methods is strongly limited by the optomechanical scanning speed, footprint, or the complexity of the control electronics.

In recent years, the use of computational imaging methods has shown promise in simplifying imaging architecture as well as enabling image reconstruction without the pixel-by-pixel scanning over the RoI. With computational imaging methods, spatially and temporally quasi-random illumination can be used to interrogate the RoI and encode information in the backscattered signal. Recently, a concept with increasing interest inside the computational imaging paradigm has been frequency-diverse imaging, as in [3]–[5]. These methods rely on swept-frequency sources and engineered frequency-dependent apertures to generate quasi-random radiation patterns. As the quasi-randomness can be applied as a feature of the radiating aperture, the number of transceivers or sensors can be reduced to the minimum. One logical progression of this approach is the "single-pixel camera" consisting of a single sensor that is multiplexed to different modes to acquire information from the target [6], [7]. These different modes can be created using random masks or coded apertures that introduce spatio-temporal modulation to the target illumination.

Various computational imaging technologies relying on the coded aperture principle have been presented in the literature. At microwave frequencies, dynamic metasurfaces have been used to actively modulate the radiation pattern at a single frequency [8] or over a narrowband [9]. Although eliminating the need for phase-shifting circuits, these methods still require

Manuscript received April 29, 2021; revised July 5, 2021; accepted July 31, 2021. Date of publication August 27, 2021; date of current version January 5, 2022. This work was supported by Research Project Arrays with DEep-Neural-Network backend for millimeter-wave beamforming applications (ADENN) through the Academy of Finland Programme ICT 2023 Beyond 5G under Grant 319770. *(Corresponding author: Samu-Ville Pälli.)*

The authors are with the MilliLab, Department of Electronics and Nanoengineering, Aalto University, 02150 Espoo, Finland (e-mail: samu-ville.palli@aalto.fi).

Color versions of one or more figures in this article are available at https://doi.org/10.1109/TMTT.2021.3106966.

Digital Object Identifier 10.1109/TMTT.2021.3106966

circuitry for active beam control. Alternatively, frequency-diverse apertures have been demonstrated at microwave and mm-wave frequencies [10]–[12]. There, varying radiation patterns were created via a simple frequency sweep, utilizing frequency-dependent metamaterial apertures or irregularly shaped cavity resonators with radiating slots. These designs, however, are rather complex and introduce challenges to accurate alignment and field characterization. Beamsteering using spatial light modulators at mm-waves has been reported in [13] and [14]. The target was scanned with a narrow beam generated by a photo-injected Fresnel-zone plate antenna. Recently, frequency-diverse mm-wave imaging with a pair of phased arrays intended for 5G base station was demonstrated in [15]. Earlier, we have demonstrated a dispersive hologram combined with a terahertz time-domain spectrometer operating at 0.1–2.0 THz and leveraged the dispersive field illumination to conduct spatial localization tasks [16].

The work presented here applies the single-pixel approach to a wideband frequency-diverse aperture. We present the design process, simulations, and experimental characterization of dual-band frequency-diverse phase holograms for distributed beamforming. The holograms served as a frequency-diverse aperture in the front end of a quasi-optical setup, modulating the phase of the incident collimated beam from a parabolic mirror. The holograms were designed to disperse the incident waves in a quasi-random way on the target at a 600 mm standoff, across frequency bands 50–75 GHz (WR-15) and 220–330 GHz (WR-3.4), while maintaining adequate diffraction efficiency. Two prototype holograms with different design parameters were manufactured, and their performance was characterized using physical-optics (PO) simulations as well as near-field measurements. The frequency diversity of the designed holograms was quantified with singular value decomposition (SVD) and correlation coefficient methods. A localization experiment was conducted using the quasi-optical setup with the manufactured hologram to acquire frequency-dependent backscatter from a corner-cube (CC) reflector translated in the field of view. A fully connected neural network was then trained to localize the CC reflector in the RoI from the back-reflected signal.

This article is organized as follows. Section II discusses the frequency-diverse beamforming method and the dispersive phase hologram. Section III introduces the synthesis process and design principles for the hologram, with Section IV presenting the PO simulation and the key performance metrics. Two manufactured hologram prototypes, the measurement setup, and the comparison of simulation and measurement results are presented in Section V. Section VI reports the results of the localization experiment using the setup with the designed hologram together with a trained neural network. Finally, conclusions and next steps are elaborated in Section VII.

II. Frequency-Diverse Imaging

Frequency-diverse imaging is a computational imaging method where spatially quasi-random field patterns are used to interrogate the RoI to acquire information from the target. The complex spatial variation of the fields is created using apertures intentionally designed to disperse the field as a function of frequency. With a simple frequency sweep, the RoI is sampled by multiple distinct measurements and the information of the target is encoded to the measured backscattered signal. Using the first Born approximation for scattered waves [17] and discretizing the RoI to pixels, the relationship between the RoI and the measured signal can be mathematically expressed as

$$\mathbf{g}_{M\times 1} = \mathbf{H}_{M\times N}\,\mathbf{f}_{N\times 1} + \mathbf{n}_{M\times 1} \tag{1}$$

where $\mathbf{g}$ is the measured backscattered signal, $\mathbf{H}$ is the measurement matrix, $\mathbf{f}$ is the reflectivity distribution of the RoI, and $\mathbf{n}$ is the system noise. Measurement matrix dimensions M and N correspond to the number of distinct measurements and the number of pixels discretizing the RoI, respectively. For a single frequency-diverse aperture, the number of distinct measurements M equals the number of points in the frequency sweep. The pixels in N are obtained by sampling the 2-D RoI with a rectilinear grid and stacked into a single vector. The measurement matrix $\mathbf{H}$ is proportional to the electric field patterns of transmitting and receiving antennas $\mathbf{H} \propto \mathbf{E}_{\mathrm{Tx}}\mathbf{E}_{\mathrm{Rx}}$ [18]. In this work, we use the same transceiver and aperture for transmitting and receiving, and thus, $\mathbf{E}_{\mathrm{Tx}} = \mathbf{E}_{\mathrm{Rx}}$.

Equation (1) ultimately describes an inverse problem of mapping an image to 2-D space using the 1-D spectral information. As is evident from the measurement matrix $\mathbf{H}$ in (1), the imaging problem can be underdetermined ($M < N$) or overdetermined ($M > N$). Thus, the measurement matrix $\mathbf{H}$ is not necessarily invertible, and reflectivity distribution $\mathbf{f}$ must be estimated using computational reconstruction techniques. A variety of computational techniques have been reported in the literature, such as matched filter [19], iterative least-squares algorithm [20], or deep neural networks [21].

A. Dispersive Phase Hologram

Holograms are diffractive elements designed to modify reflected and transmitted electromagnetic fields. A simple hologram is essentially a locally periodic diffraction grating, shaping the incident field to a desired reflected or transmitted field at a designed frequency, e.g., incident spherical wave to transmitted plane wave, as in [22] and [23]. Holograms can be divided into amplitude- and phase-type holograms depending on the primary property of modulation. This work focuses on transmission-type phase holograms, consisting of low-loss dielectric material with spatially varying electrical thickness to introduce phase differences to the transmitted field. In general, phase holograms possess higher diffraction efficiency in comparison to amplitude holograms, where the incident field is partially blocked by conductive sections [24].

Typical radio-wave phase holograms are designed to planarize or focus on the transmitted field at a single frequency with high accuracy [25]. However, the purpose of a frequency-diverse phase hologram is to disperse the incident field with maximum spatial variation at the RoI over a wide illumination band while preserving high diffraction efficiency. This is realized by synthesizing a surface structure with quasi-random transverse distribution in electrical length. As the

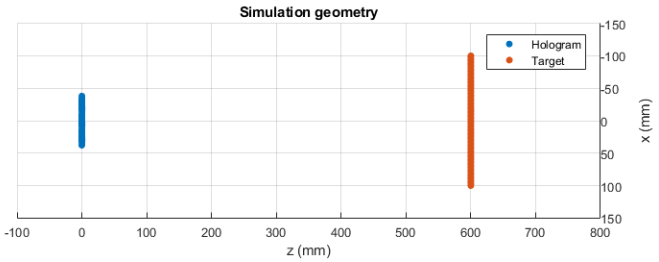

Fig. 1. Simulation geometry for hologram synthesis.

illumination frequency is varied, phase shifts from different elementary areas interfere constructively or destructively at different locations creating spatially varying field patterns at the RoI. The ability to utilize the entire waveguide bandwidth enhances the imaging performance as the number of distinct measurements increases. In practice, maximizing the beam dispersion and diffraction efficiency is mutually exclusive, and the determination of the hologram structure becomes an optimization problem.

III. Synthesis and Design of Holograms

A. Hologram Synthesis

An in-house developed PO simulation code was used to find a hologram design suitable for operating at frequency bands of 50–75 and 220–330 GHz and to synthesize the phase hologram. The code follows the formalism of calculating radiating fields from a finite aperture to another finite surface [26]. The synthesizing process creates the surface structure that will produce the quasi-random field patterns. The PO simulation used in the hologram generation consists of two on-axis simulation planes, namely "hologram" and "target," as shown in Fig. 1. The rectilinear dimensions of the hologram plane and the target plane were $D_{x,h} = D_{y,h} = 76.2$ mm and $D_{x,t} = D_{y,t} = 200$ mm, respectively.

The hologram plane sample spacing was $d_{x,h} = d_{y,h} = 0.3$ mm corresponding to less than $\lambda/2$ at the highest operating frequency of 330 GHz. The target plane has a coarser sampling grid of $d_{x,t} = d_{y,t} = 2.0$ mm to limit the simulation time.

First, the goal electric field with random amplitude and phase distribution was created at the target plane at a chosen design frequency f_{design}. This design frequency is not directly related to the intended operating frequency of the hologram but instead affects the detail size of the hologram surface structure. The random goal field serves as an ideal model of a dispersive field following diffraction from the hologram, albeit physically unrealizable for the small hologram aperture. The goal field is defined as

$$E_{\text{goal}} = \sqrt{R}_{i,j} e^{j2\pi P_{i,j}} \tag{2}$$

where $(R)_{i,j}^{1/2}$, $R_{i,j} \in U(0,1)$ and $P_{i,j} \in U(0,1)$ represent the random amplitude and phase variables, respectively. This random field distribution is then computationally backpropagated to the hologram plane to give the field distribution pattern, at the hologram plane, which would realize the random goal field at the target plane. The method follows the formalism of calculating the electric field outside radiating apertures [27]:

$$\mathbf{E}(\mathbf{r}, k_{\text{design}}) = -\oint_S \nabla G(\mathbf{r} - \mathbf{r}', k_{\text{design}}) \times \mathbf{J}_{\text{ms}}(\mathbf{r}', k_{\text{design}}) dS \tag{3}$$

where $\mathbf{r}$ and $\mathbf{r}'$ are the locations on the radiating aperture and at the observation point, respectively, G is the scalar Green's function, and $\mathbf{J}_{\text{ms}}$ is the magnetic surface current density. The field has the wavenumber of $k_{\text{design}} = 2\pi f_{\text{design}}/c_0$, where f_{design} is the design frequency of the hologram. The resulting field at the hologram plane now has a quasi-random amplitude and phase distribution, with the transverse detail size dictated by the chosen design frequency. An example of the random goal field distribution at the target plane and its backpropagated field at the hologram plane is shown in Fig. 2(a)–(d).

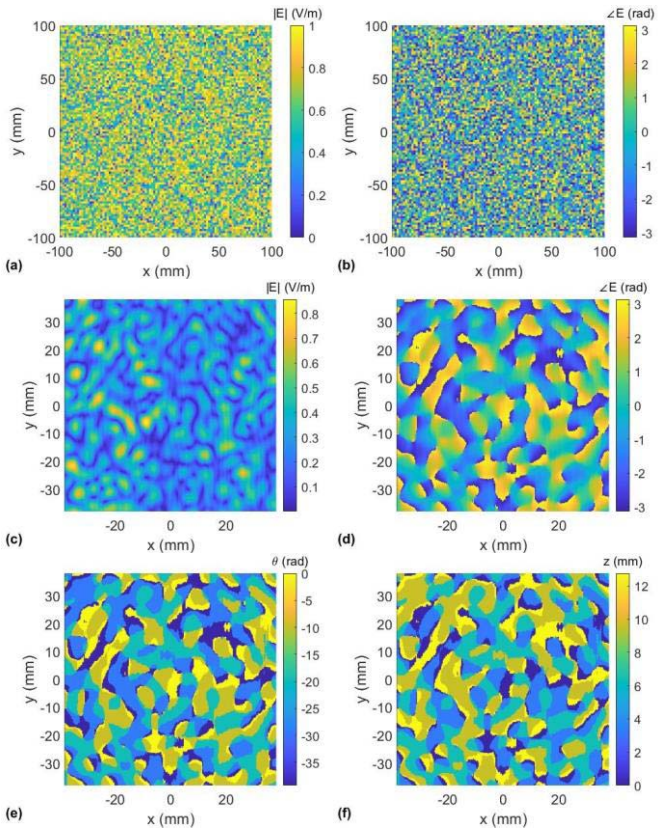

Fig. 2. Example of a random goal E-field (a) amplitude and (b) phase when synthesizing the hologram. This field is backpropagated onto the hologram plane, creating the following (c) amplitude and (d) phase pattern. (e) Phase pattern of (d) (in radians) after discretization using (4). (f) Calculated depth profile for the hologram (in mm).

Second, the phase of the calculated field distribution at the hologram plane is discretized so that ideally, the hologram profile introduces a phase shift defined as

$$\theta_{h,\text{discr}} = (q + m)\,\text{round}\left(\frac{\theta_{h,\text{cont}}}{q}\right) \tag{4}$$

where $\theta_{h,\text{cont}}$ is the continuous calculated phase distribution determined at the chosen design frequency at the hologram plane and q and m are hologram design parameters for phase quantization step and added phase, respectively. In practice,

the high aspect ratio of surface details causes complex propagation and shadowing that affect the realized phase. After the discretization, the resulting phase pattern is then converted to a corresponding distribution in dielectric material thickness at transverse positions (x, y) at the design frequency f_{design} using

$$z_{h(x,y)} = \frac{-\theta_{h,\text{discr}(x,y)}}{\left(\sqrt{\varepsilon}_{r,h} - 1\right)k_{\text{design}}} \tag{5}$$

where $\varepsilon_{r,h}$ is the relative permittivity of the hologram material and k_{design} is the wavenumber at the design frequency f_{design}.

It is important to note that accurate knowledge of the hologram material relative permittivity is needed to ensure that the manufactured hologram operates as intended. Fig. 2(e) and (f) shows an example of a discretized phase pattern and a corresponding hologram depth profile realizing this phase shift. As is evident from (4), the quantization step q dictates the number of discrete electrical depths in the structure. Using a tiny quantization step quickly results in excessively smooth phase variation, which can impose challenges when manufacturing the structure. The added phase m is used to increase the phase modulation over the illumination frequency range and thus greatly affects the overall depth of the structure, as seen from (4) and (5).

Finally, to simulate the properties of the synthesized hologram, the hologram structure is illuminated by a collimated TEM_{00} Gaussian beam at the hologram plane, and the resulting electric field at the target plane is calculated using (3). The depth variation of the hologram structure modulates the incident phase resulting in a quasi-random field pattern at the target plane. The calculated field distributions at the target plane are used to analyze the field behavior over a wide frequency band.

B. Bandwidth Tuning

In a synthesized hologram with fixed design parameters, the effective electrical pathlength varies in different transverse locations, as shown in Fig. 2(f). As the frequency of the beam illuminating the hologram is varied, wavefronts emanating from each elementary hologram area sum up differently, resulting in frequency-diverse field patterns at the target plane. By analyzing the fields at the target plane over a wide frequency band (30–400 GHz) with holograms of varying design parameters, a relation between the design parameters and the target field behavior was found. Frequencies where the target field maintains the approximate input Gaussian amplitude pattern, i.e., where the hologram does not cause dispersion to the incident field, can be calculated from

$$f_{\text{ND}} = \frac{f_{\text{design}}}{q + m}\, 2\pi N, \quad N = 0, 1, 2, \ldots \tag{6}$$

where f_{ND} is the center frequency where a nondispersive field occurs, f_{design} is the hologram design frequency, q is the phase quantization step, and m is the added phase. The outcome of (6) is further explained in Fig. 3. Fig. 3(a) shows a table of calculated nondispersive frequencies using (6) for a hologram with design parameters of $f_{\text{design}} = 120$ GHz, $q = \pi/2$, and $m = 1.9\pi$. Fig. 3(b) shows the simulated electric field amplitude pattern at the target plane for the corresponding hologram.

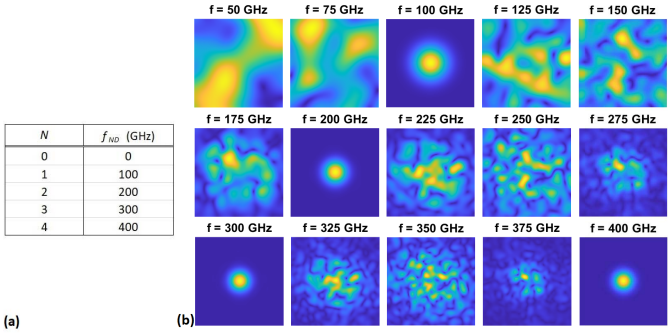

Fig. 3. (a) Example of nondispersive frequencies f_{ND} calculated using (6) for a hologram with design parameters of $f_{\text{design}} = 120$ GHz, $q = \pi/2$ and $m = 1.9\pi$. (b) Simulated electric field pattern at the target plane for the same hologram at selected frequencies.

From Fig. 3, it is evident that the field does not disperse at the calculated nondispersive illumination frequencies of $N \times 100$ GHz, where N is an integer number. At frequencies given by (6), the phase difference generated by each distinct phase level of the hologram equals to $N \times 2\pi$ radians at an arbitrary plane beyond the hologram. As there is no relative phase difference, the incident field is retained after the hologram. In practice, the complex propagation and shadowing results in minor modulation.

In the bands lying in-between these nondispersive frequencies, the fields are dispersed and rapidly varying with illumination frequency. Since the frequencies where the nondispersive fields exist can be calculated, it is possible to adjust the design parameters f_{design}, q, and m so that the nondispersive frequencies do not fall within the desired operating frequency bands of the hologram. This relationship suggests that a single hologram can be designed to operate at multiple frequency bands, where the chosen design parameters impose limitations on the bandwidth.

C. Design Overview

The flowchart in Fig. 4 summarizes the hologram design process. Before starting the synthesis process described in Section III-A to create the hologram structure, the design parameters are chosen to match with the desired operating frequency of 50–75 GHz and 220–330 GHz with help of (6). This minimizes the number of nondispersive frequencies inside the desired operation band. Potential issues with manufacturability can be compensated by tweaking the quantization step q and added phase m. After a hologram with sufficient operation frequency band and manufacturability is identified, full quasi-optical simulations are performed to characterize its efficiency and dispersion. The computation time for the process shown in Fig. 4 is less than 1 min with a modern desktop computer.

IV. Full-Quasi-Optics Simulations

Two holograms with different design frequencies and added phases were synthesized to evaluate the performance between differing designs. The quantization step was chosen as $q = \pi/2$ for both designs to ensure manufacturability. For the purpose to interrogate the RoI, diffraction efficiency and

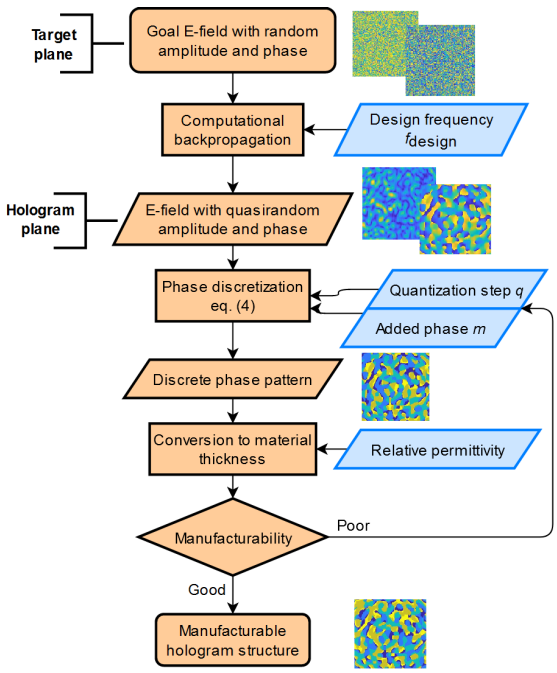

Fig. 4. Flowchart of the hologram design process. The input design parameters (blue rhomboids on the right) should be matched to the desired operating frequency band before the process using (6).

TABLE I
DESIGN PARAMETERS OF BOTH HOLOGRAM DESIGNS

Hologram no.	q (rad)	m (rad)	f_{design} (GHz)
1	$\pi/2$	1.9π	120
2	$\pi/2$	3π	300

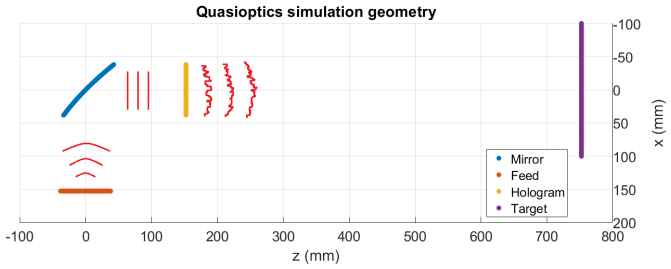

Fig. 5. Simulation geometry to analyze the performance of the holograms. A Gaussian beam originating from the feed plane is collimated using the OAP mirror. The hologram modulates the incident wavefront, and the resulting field pattern is analyzed at the target plane.

frequency diversity were considered the most critical performance metrics. Both holograms were designed to produce frequency-diverse fields in the 50–75 and 220–330 GHz bands. All design parameters for both holograms are shown in Table I.

A. Simulation Geometry

The PO simulation geometry was updated to resemble the actual measurement setup. The simulation consisted of four calculation surfaces, as shown in Fig. 5. Instead of assuming ideal illumination at the hologram surface, a Gaussian beam was generated at the feed plane, modeling an mm-wave transceiver with a Pickett–Potter horn antenna. The electric field of the Gaussian beam originating from the feed plane was defined as

$$E_{\text{feed}}(r_f) = \mathbf{u}_y e^{-r_f^2/w_0^2} \tag{7}$$

where r_f is the radius from the center axis of the beam and w_0 is the beam waist radius. The field in (7) was propagated to the surface of a 76.2 mm in diameter clear aperture, 76.2 mm parent focal length, and 90° off-axis parabolic (OAP) mirror to collimate the incident beam. The OAP mirror was located at a distance of 2×76.2 mm $= 154.2$ mm from the feed plane along the optical axis, corresponding to the effective focal length of the mirror. The resulting field was propagated to the hologram surface at 154.2 mm from the mirror along the optical axis. The varying thickness of the hologram modulated the incident field so that the field emanating from the hologram was

$$\mathbf{E}_{\text{hol}}(x, y) = \mathbf{E}_{\text{hi}}(x, y) e^{-\frac{1}{2}k_0 z_h(x,y)\delta_h \sqrt{\varepsilon}_{r,h}} e^{-jk_0 z_h(x,y)(\sqrt{\varepsilon}_{r,h}-1)} \tag{8}$$

where $\mathbf{E}_{\text{hi}}$ is the electric field incident on the hologram, k_0 is the free-space wavenumber, $z_h(x, y)$ is the hologram dielectric thickness, and δ_h and $\varepsilon_{r,h}$ are the loss tangent and the relative permittivity of the hologram material, respectively.

Finally, the electric field $\mathbf{E}_{\text{hol}}$ was propagated to the target plane located 600 mm from the hologram. Simulations were performed over both frequency bands 50–75 and 220–330 GHz with steps of 1 GHz. The simulation time for one frequency point was on the order of minutes but was strongly dependent on the size and sample spacing of the calculation surfaces.

B. Diffraction Efficiency

The diffraction efficiency of a hologram is defined as the ratio of power over the RoI with the hologram present divided by the power incident on the hologram or

$$\eta = \frac{\sum_N \left[|E_{\text{roi}}|^2 dA\right]}{\sum_N \left[|E_{\text{inc}}|^2 dA\right]} \tag{9}$$

where E_{roi} and E_{inc} are the electric fields calculated at the RoI with and without hologram present, respectively, $dA = dx \times dy$ is the elementary area, and N is the number of samples discretizing the RoI. Edge effects from the high aspect ratio and sharp corners in the hologram structure disperse the power outside the RoI although the total energy in the edge diffracted beams was assumed negligible. In addition, transmission loss had a minor effect on the overall efficiency of the hologram.

C. Frequency Diversity

The frequency diversity of a hologram describes the lack of correlation in spatial field distribution in the RoI between different illumination frequencies. The similarity in field patterns at different frequencies leads to overlapping information content and reduces the overall information that can be extracted from target reflection. Here, two different metrics for frequency diversity of the measurement matrix were used: correlation coefficient and SVD. The correlation coefficient gives the linear dependence of field patterns between two

frequencies and is calculated from the complex-valued field vectors containing the electric field at all sampling points in the RoI. The correlation coefficient of two electric field patterns is defined as

$$\rho(E_1, E_2) = \left| \frac{\text{cov}(E_1, E_2)}{\sigma_{E1}\sigma_{E2}} \right| \tag{10}$$

where E_1 and E_2 are complex-valued vectors containing the electric field at all sampling points in the RoI, respectively, σ_{E1} and σ_{E2} are the standard deviations of E_1 and E_2, respectively, and $\text{cov}(E_1, E_2)$ is the covariance of E_1 and E_2. To better illustrate the correlation between different frequency points, the correlation coefficients are mapped as 2-D surface plots, where the absolute value of the correlation coefficient between fields at frequencies is in the x-axis and y-axis. The correlation coefficient of 1 indicates perfect linear dependence and 0 means no linear relationship between two matrices. The extent of low correlation coefficient values outside the unity diagonal in the surface plots indicates higher frequency diversity in the field patterns and vice versa.

The SVD is a mathematical tool to assess the diversity of field patterns created by the hologram [28]. For the measurement matrix $\mathbf{H}$, the SVD can be written as

$$\mathbf{H}_{M\times N} = \mathbf{U}_{M\times M}\mathbf{\Sigma}_{M\times N}\mathbf{V}^T_{N\times N} \tag{11}$$

where $\mathbf{U}$ and $\mathbf{V}$ are unitary matrices, $(\cdot)^T$ denotes matrix transpose, and $\mathbf{\Sigma}$ is a diagonal matrix containing singular values $\sigma_1, \sigma_2, \ldots, \sigma_m$ of the measurement matrix $\mathbf{H}$ in descending order. The diversity of the measured fields can be analyzed from the decay rate of the singular value spectrum. A rapidly decaying singular value spectrum indicates a high correlation between measurements and, thus low diversity, whereas a flat spectrum is a sign of high diversity between the measurements.

V. Experimental Work and Results

A. Manufactured Holograms

Holograms #1 and #2 were computer numerical control (CNC)-machined from 30-mm-thick blocks of low-loss cross-linked polystyrene (Rexolite 1422, $\varepsilon_r \approx 2.52 - j0.0005$) [29]. The material was chosen for its good manufacturability and low loss at millimeter and submillimeter wavelengths. The material used for the hologram can be selected freely as long as its electrical properties are known before the synthesizing process. The aperture size of both holograms was 76.2 × 76.2 mm^2. Fig. 6 shows the designed structures together with the manufactured holograms. The manufacturing accuracy is limited by the 1-mm diameter of the cutting tool and thus does not allow for the perfect realization of the synthesized design in Fig. 5(a) and (b). In addition, tall and thin details are prone to break during the machining process, and thus, feature height was constrained during the design process. Overall, we believe that the manufacturing limitations have limited contribution to the hologram performance. Manufacturing process limitations could be addressed with alternative techniques, such as 3-D-printing. Hologram #1 had a surface

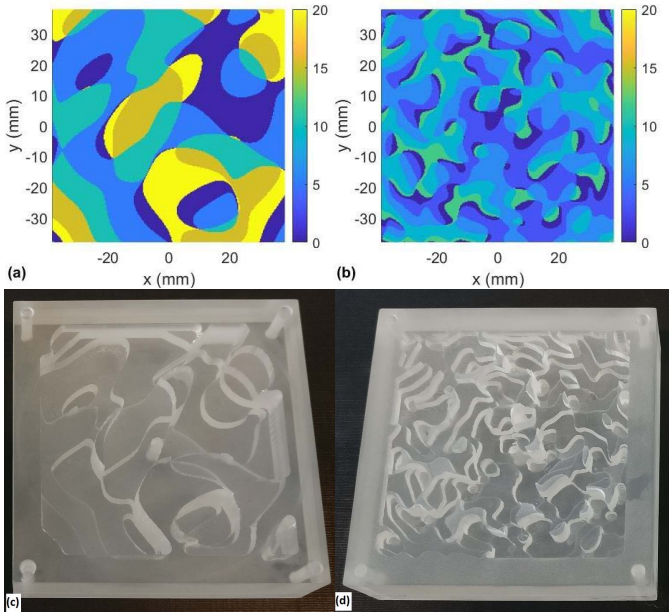

Fig. 6. Surface plots of the hologram structures (in mm). (a) Hologram #1. (b) Hologram #2. Structures manufactured on Rexolite. The overall dimension of the manufactured block is 94 × 94 mm. (c) Hologram #1. (d) Hologram #2.

structure step height of 5.1 mm, corresponding to 1.3–2.0 wavelengths from 50 to 75 GHz and 5.9–8.9 wavelengths from 220 to 330 GHz. The step height of hologram #2 was 3.0 mm, corresponding to 0.8–1.2 wavelengths from 50 to 75 GHz and 3.5–5.2 wavelengths from 220 to 330 GHz.

B. Measurement Setup

The holograms were measured with an N5225A PNA Microwave Network Analyzer (Keysight Technologies, Inc.), referred to in the remaining text as a vector network analyzer (VNA). The VNA drives millimeter-wave extenders WR15-VNAX and WR3.4-VNAX (Virginia Diodes Inc.) to achieve the measurement frequency bands of 50–75 and 220–330 GHz, respectively. The transceiver VNA extension modules (VNAX) were coupled to the Pickett–Potter dual-mode horn antennas (Radiometer Physics GmbH) for the corresponding frequency range. The horn antennas serve as a Gaussian radiation source for the OAP collimating mirror (Edmund Optics). The OAP mirror had a diameter of 76.2 mm and an effective focal length of 127 mm. An open-ended waveguide (OEWG) for the corresponding frequency range was used as a probe antenna coupled to the VNAX receiver module. The VNAX receiver was mounted on a planar near-field scanner (NSI-200 V-5 × 5 by Near-Field Systems Inc.) to perform the xy scanning in the measurement plane.

The measurement setup was built on two separate optical breadboards on an optical table. Before the measurements, the VNAX transceiver module with the horn antenna was aligned with the OAP mirror by scanning the field without the hologram present. Once the measured phase front demonstrated sufficient planarity, the VNAX transceiver module was fixed in place, and the hologram was secured to its mount. The resulting distance of the horn antenna phase center was

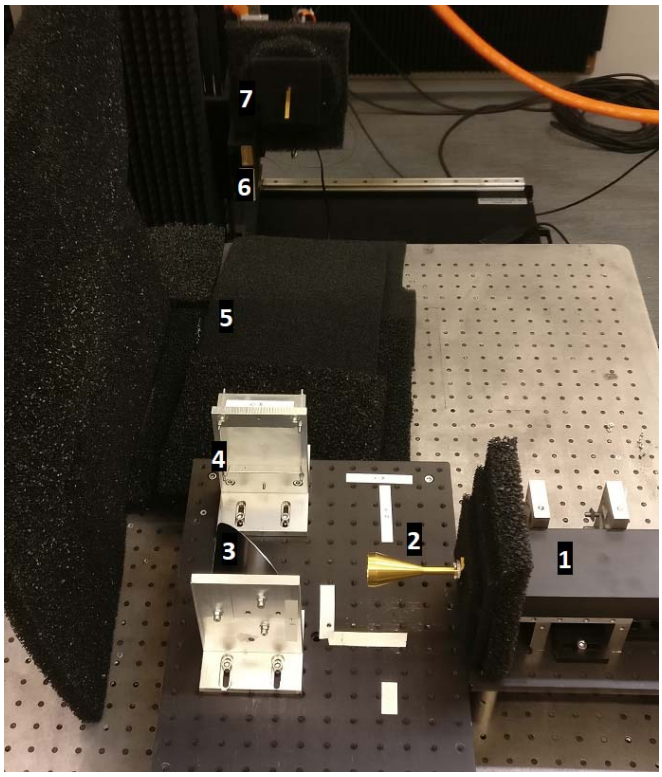

Fig. 7. Measurement setup for hologram field pattern measurements at 50–75 GHz. 1) WR15-VNAX transceiver; 2) Pickett–Potter horn antenna; 3) OAP mirror; 4) hologram; 5) RAM; 6) planar near-field scanner; and 7) OEWG probe antenna connected to WR15-VNAX receiver (behind RAM).

slightly less than the effective focal length from the mirror along the optical axis at both frequency ranges. The distance between the OAP mirror and the hologram was fixed at 154.2 mm. The distance from the hologram surface to the OEWG at the receiver was 600 mm. The structural planarity of the components and the probe antenna at the scanning area origin was confirmed with a line laser. Flat surfaces near the measurement setup were covered with radar-absorbing material (RAM) to prevent multipath propagation and unwanted reflections. The complete measurement setup is shown in Fig. 7.

At 220–330 GHz, the measurement scanning plane was 200×200 mm^2 in size with a sampling interval of 2.0 mm, resulting in 101×101 S_{21} measurements. At the lower frequency range, the scanning area was limited to 300×300 mm^2 due to the available tablespace. The spatial sampling interval at 50–75 GHz was 3.0 mm, preserving the 101×101 measurements. In both frequency bands, the frequency sampling step was 50 MHz, resulting in 501 and 2201 frequency points for the lower and higher frequency bands, respectively.

C. Field Patterns

Fig. 8 shows a detailed comparison of simulated and measured target fields for hologram #1 at selected frequency points. At 55 GHz, the measured field pattern shows all eight maxima of the simulated field, although not as distinctly.

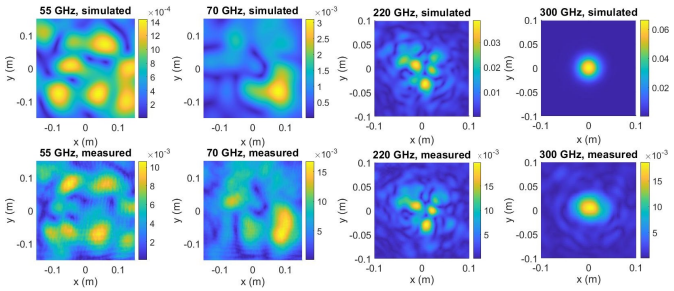

Fig. 8. Detailed comparison of simulated and measured target field patterns for hologram #1 at selected frequencies. The absolute values of simulated E-field strength and measured S_{21} amplitude in colorbars are not directly comparable.

At 70 GHz, the measured field has three clear maxima compared to only one in the simulated field but both share the distinct inverted S-shaped minima around the center. The field pattern at 220 GHz demonstrates the increased similarity between the simulated and measured fields, with three narrow beams clearly present in the center of the RoI. Comparison at a nondispersive frequency of 300 GHz illustrates the subtle difference to idealized simulation, as the dual-mode horn antenna does not generate a perfect Gaussian beam at 300 GHz, and some spatial dispersion is visible around the main beam. Moreover, edge effects and shadowing in the hologram add minor nonidealities. Overall, the observed similarity between simulated and measured fields indicates that the PO simulation is suitable for analyzing the field distribution created by the hologram to sufficient accuracy for both illumination bands. The designed and measured phase profile for hologram #1 was studied with near-field planar scanning at 275 GHz, and the results show good agreement with an average error of less than 6° [30].

D. Efficiency

Measured efficiencies for both holograms at both frequency bands are presented in Fig. 9 with the simulated results. The simulated efficiencies were calculated over the same area as the measurements using (9). At 50–75 GHz, the measured and simulated efficiencies are similar, and the measured values for hologram #2 agree with the simulated values. At 220–330 GHz, the simulated efficiency is noticeably higher than the measured efficiency. However, the increasing trend of simulated values is not visible at all in measured values.

The ideal beam propagation in the simulations, assuming no multiple reflections and shadowing, may explain the difference between simulated and measured efficiencies. The sharp edges on the hologram surface pattern likely cause diffraction, and some fraction of the power is directed away from the RoI. For more accurate efficiency characterization, the target plane should have a larger area so that the power that spills over the target plane is negligible. This is especially the case with the measurements at the lower frequency band, as the field intensity was still significant at the scanning area edges. For example, the spillover is pronounced for hologram #1 at

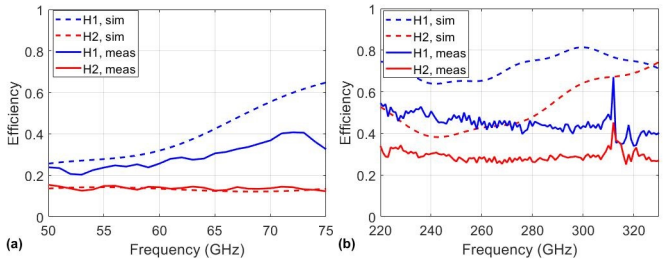

Fig. 9. Measured and simulated efficiencies for both holograms at (a) 50–75 and (b) 220–330 GHz. The clear spikes in measured values between 310 and 320 GHz are measurement artifacts.

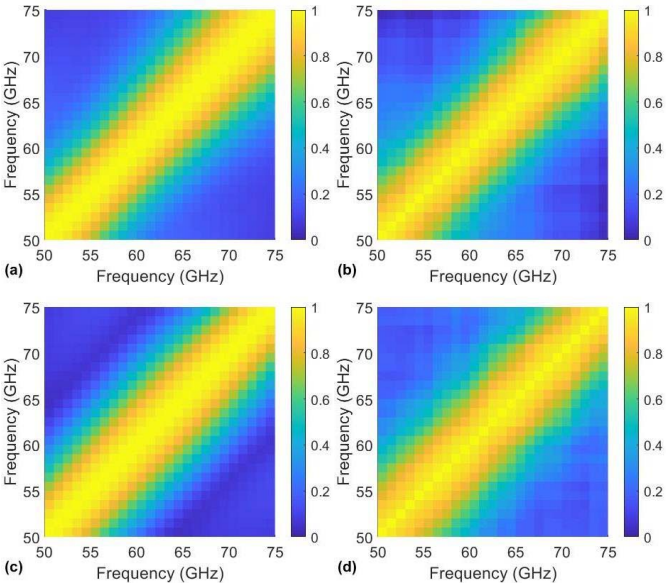

Fig. 10. Correlation coefficients of 26 frequency-diverse field patterns at 50–75 GHz. Hologram #1 (a) simulated and (b) measured. Hologram #2 (c) simulated and (d) measured.

55 GHz in Fig. 8. However, practical constraints prevented a sufficiently large, measured target plane. Although less than simulated, the measured efficiency of 20%–40% at 50–75 GHz and 40%–50% at 220–330 GHz for hologram #1 was considered satisfactory for the localization experiments.

E. Frequency Diversity

Figs. 10 and 11 show the correlation coefficient plots of both measured and simulated complex field patterns for both holograms at 50–75 and 220–330 GHz, respectively. Horizontal and vertical lines visible around 310–320 GHz in Fig. 11(b) and (d) are measurement artifacts. Correlation coefficients show good agreement between simulated and measured data. Correlation between the fields seems to drop below 0.5 beyond ∼10 GHz of difference in frequency, indicating better imaging performance at the wider frequency band of 220–330 GHz. However, there seems to be no significant difference in frequency diversity between the two hologram designs. The yellow diagonal is slightly thinner for the measured hologram #1 at 220–330 GHz and also

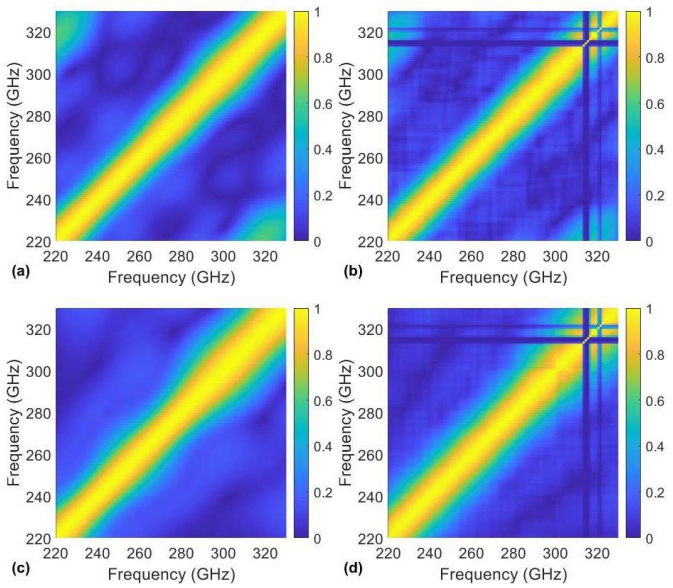

Fig. 11. Correlation coefficients of 111 frequency-diverse field patterns at 220–330 GHz. Hologram #1 (a) simulated and (b) measured. Hologram #2 (c) simulated and (d) measured. Horizontal and vertical lines at 310–320 GHz in (b) and (d) are measurement artifacts.

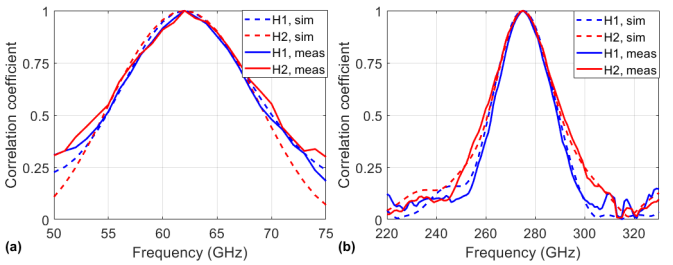

Fig. 12. Cross sections of correlation coefficient plots in Figs. 10 and 11 at (a) 62 and (b) 275 GHz. Measured hologram #1 demonstrates slightly lower correlation at both bands.

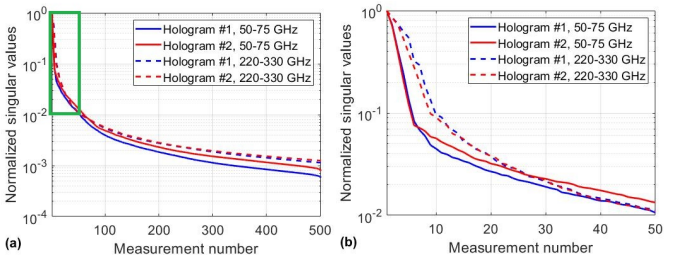

Fig. 13. (a) Normalized singular value spectra of 501 measured field patterns both holograms at 50–75 and 220–330 GHz. (b) Highlighted window presenting the difference in initial decay of singular values.

exhibits slightly lower correlation values further away from the diagonal, more visible in the cross sections in Fig. 12. The similarity in frequency diversity is also evident from Fig. 13, which shows the singular value spectra of measured fields for both holograms over both frequency bands. Apart from the initial decay, both holograms share a similar decay rate over both frequencies, indicating similar frequency diversity.

TABLE II
KERAS SUMMARY OF THE NEURAL NETWORK TOPOGRAPHY

Layer	Output shape	Param #
FC1	1000	2003000
Dropout	1000	0
FC2	500	500500
FC3	100	50100
FC4	50	5050
FC5	25	1275
FC6	10	260
FC7	2	22

Total params: 2,560,207
Trainable params: 2,560,207
Non-trainable params: 0

VI. LOCALIZATION EXPERIMENTS WITH NEURAL NETWORK

To demonstrate the performance, the holograms were utilized in a localization task with a CC reflector. The aluminum CC had a diameter of 12.5 mm and represents a highly reflective, point-like target in the RoI. The CC was scanned in the RoI in the same area where the S_{21} measurements were carried out (Fig. 7). The back reflection (S_{11} parameter) was recorded at each location in 501 (WR-15) and 2201 (WR-3.4) frequency points. The measured S_{11} parameter was processed by removing the mean value and time gating.

After processing, the S_{11} parameter was min-max normalized and arranged in a 2002-element vector consisting of 1001 real and 1001 imaginary components of the processed S_{11} parameter. A fully connected neural network was trained with the processed data, totaling 10 000 CC positions. The x- and y-coordinates of the CC were used as labels to the neural network. The neural network was trained in Keras deep-learning API [31]. The fully connected network consisted of six hidden layers. A dropout layer with a probability of 50% was used in training to prevent overfitting. The learning rate was set to 0.001 in the Adam optimizer. The Keras summary of the neural network topography is shown in Table II.

The loss function in training was the mean squared error of the localization. The network was validated with mean absolute error (MAE) similar to the Manhattan distance of predictions and labels. Fig. 14 shows the training loss and validation MAE. As indicated by the SVD and correlation-coefficient characterization of the dispersed fields, hologram #1 outperforms both in training loss and validation MAE.

A. Localization Performance

Localization error was defined as the Euclidean distance between the predicted and the true position. The true and predicted locations of the CC as well as the error vectors are shown in Fig. 15. The largest errors are observed with hologram #2 at both bands. With hologram #1, the error is smaller. Some of the errors at WR-3.4 are as significant as at WR-15. The minimum average error seems to occur at WR-3.4

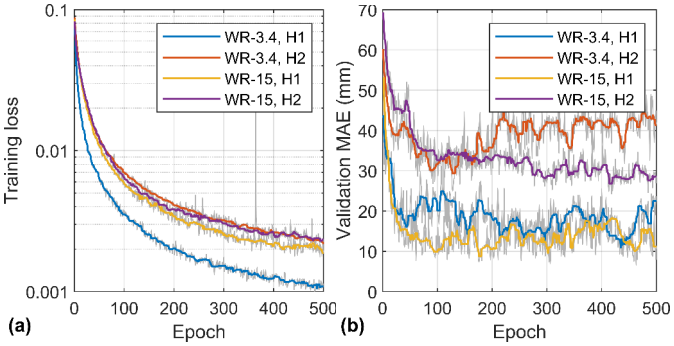

Fig. 14. (a) Loss during training of the fully connected neural network. The loss with hologram #1 at WR-3.4 outperforms, while the loss is highest with hologram #2 at both bands. (b) Validation MAE for the holograms shows the best performance for hologram #1 at both bands.

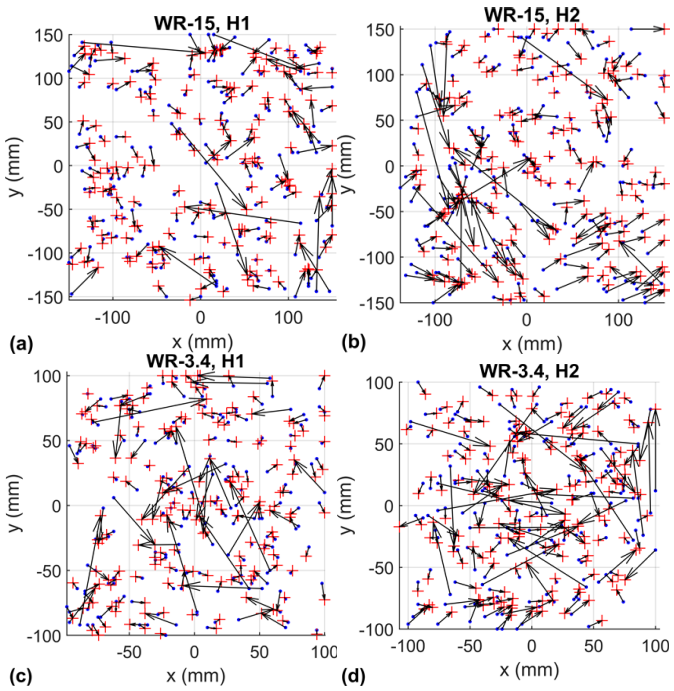

Fig. 15. CC location predictions (red cross) compared to the true locations (blue dots) for both holograms at (a) and (b) WR-15 and (c) and (d) WR-3.4. The error vector is shown with the black arrows.

as evidenced by the statistical data shown in Fig. 16. The mean localization error and variance are clearly the smallest for hologram #1 at WR-3.4. The localization statistics are shown in Table III for both bands and holograms. The statistics show that the localization error correlates with the law of diffraction: the errors are smaller at the higher frequency band. At WR-15, the CC diameter is two wavelengths at minimum, and at WR-3.4, it is 13 wavelengths at maximum. The large size of the CC aperture, especially at WR-3.4, may result in ambiguity in defining the resolution: the CC is not an isotropic scatterer and may not represent point-like featureless target.

The localization error can be compared to the diffraction-limited focused Gaussian beams. The average edge taper in the hologram aperture is 6 and 28 dB at WR-15 and WR-3.4,

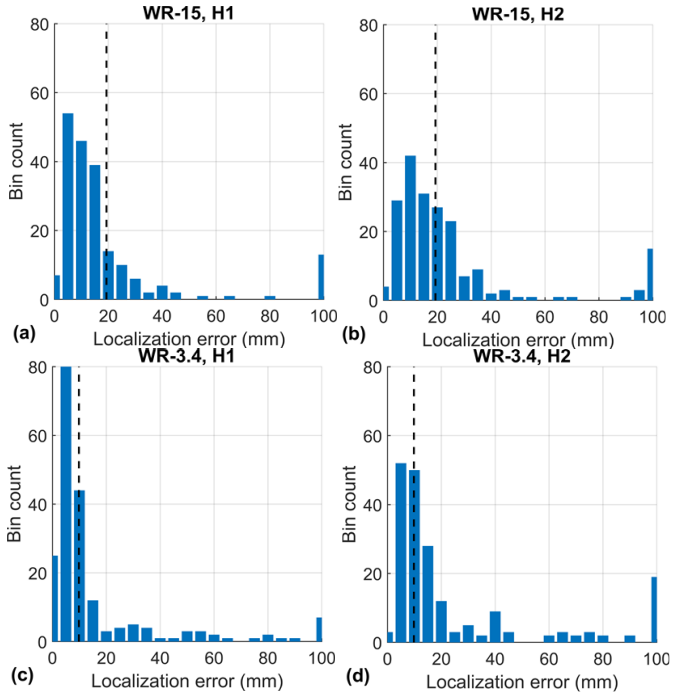

Fig. 16. Histograms of localization error in validation step for both holograms at (a) and (b) WR-15 and (c) and (d) WR-3.4. Vertical dashed line shows the equivalent Gaussian-beam waist radius. The localization accuracy is below the theoretical waist radius in most cases.

TABLE III
LOCALIZATION ERROR FOR THE HOLOGRAMS AT WR-15 AND WR-3.4

	Hologram #1		Hologram #2	
	WR-15	WR-3.4	WR-15	WR-3.4
Mean (mm)	24	17	30	30
Std. (mm)	42	30	45	44

respectively. Following [32], the Gaussian-beam radius at the aperture is:

$$w = \sqrt{\frac{8.686}{T[\text{dB}]}}\frac{D}{2} \tag{12}$$

where $D = 76.2$ mm is the dimension of the aperture and T is the edge taper. The Gaussian-beam radius at the aperture is 46 mm at WR-15 and 21 mm at WR-3.4. For focused beam, the resulting Gaussian-beam waist radius at the localization distance $z = 600$ mm is

$$w_0 = \sqrt{\frac{w^2}{2}\left\{1 \pm \sqrt{1 - \left(\frac{2\lambda z}{\pi w^2}\right)^2}\right\}} \tag{13}$$

giving waist radii of 23 and 12 mm at WR-15 and WR-3.4, respectively. In [1], the two-way resolution of an imaging radar is reported to be

$$\delta = \frac{\text{FWHM}}{\sqrt{2}} = \frac{2\sqrt{\ln(2)w_0^2}}{\sqrt{2}} \tag{14}$$

where FWHM is full-width at half-maximum. The resolution is $\delta = 27.3$ mm and $\delta = 13.9$ mm at WR-15 and WR-3.4, respectively. These theoretical limits are shown with dashed lines in Fig. 16. The comparison to ideal two-way resolution shows that the average localization accuracy is on par with the conventional focused systems especially for hologram #1 at WR-3.4.

VII. DISCUSSION AND CONCLUSION

This article presented a dual-band, frequency-diverse phase hologram for distributed beamforming. The hologram structure was synthesized using PO simulations and was designed to produce quasi-random field patterns at 50–75- and 220–330-GHz frequency bands. The hologram occupied the front end of an mm-wave quasi-optical setup, where the complex surface pattern of the hologram created multiwavelength phase shifts across the wide bandwidth resulting in spatially varying field patterns at the RoI. Two holograms with different design parameters were manufactured from Rexolite and characterized in terms of diffraction efficiency and frequency diversity using PO simulations and verified experimentally with near-field measurements. In addition, experiments to localize a CC reflector in the RoI using the hologram combined with a fully connected neural network were conducted to demonstrate the applicability to mm-wave imaging.

Both the PO simulations and the experimental results suggested that the manufactured hologram #1 outperformed hologram #2 in terms of diffraction efficiency and frequency diversity over both frequency bands. The design parameters for hologram #1 were the design frequency of 120 GHz, the phase quantization step of $\pi/2$ radians, and the added phase of 1.9π radians. The measured efficiency of hologram #1 was 20%–40% at 50–75 GHz and 40%–50% at 220–330 GHz. The measured efficiency is better or on par with microwave frequency-diverse metasurfaces and the W-band cavity-fed metasurfaces reported in [5], [12], and [33].

Both the correlation coefficients or the singular value distributions calculated from the complex field matrices did not indicate significant differences in frequency diversity between the holograms. However, the localization accuracy of hologram #1 was clearly superior, especially at the higher frequency band (220–330 GHz). Frequency diversity quantified with correlation coefficients and singular value spectrum was lower compared to other frequency-diverse apertures reported in the literature, such as [4], [12], [19]. These methods utilize complex propagation from resonating elements to achieve high diversity in relatively narrowband. The phase modulation principle used by the hologram imposes a challenge on creating rapidly changing fields, which is compensated by the wide operation band to achieve adequate frequency diversity.

The presented frequency-diverse phase hologram provides a low-cost method for producing quasi-random spatially varying field patterns at millimeter and submillimeter-wave frequencies. The design allows easy manufacturing with CNC or 3-D-printing techniques and is scalable in size and frequency. The generated field patterns have sufficient frequency diversity to encode spatial information about the target to the measured

reflected signal, as demonstrated by the localization experiments. We believe that the localization task of a 1-D target can be extended to imaging of more complex targets in the future.

ACKNOWLEDGMENT

All millimeter-wave experiments have been carried out in MilliLab, an external laboratory of the European Space Agency. The simulations presented above were performed using computer resources within the Aalto University School of Science "Science-IT" Project. Markus Grönholm from Alshain Oy is thanked for the hologram manufacturing.

REFERENCES

[1] K. B. Cooper, R. J. Dengler, N. Llombart, B. Thomas, G. Chattopadhyay, and P. H. Siegel, "THz imaging radar for standoff personnel screening," *IEEE Trans. THz Sci. Technol.*, vol. 1, no. 1, pp. 169–182, Jun. 2011.

[2] S. S. Ahmed, A. Schiessl, and L.-P. Schmidt, "A novel fully electronic active real-time imager based on a planar multistatic sparse array," *IEEE Trans. Microw. Theory Techn.*, vol. 59, no. 12, pp. 3567–3576, Dec. 2011.

[3] T. V. Hoang *et al.*, "Spatial diversity improvement in frequency-diverse computational imaging with a multi-port antenna," *Results Phys.*, vol. 22, Mar. 2021, Art. no. 103906.

[4] M. Zhao *et al.*, "Frequency-diverse metamaterial cavity antenna for microwave coincidence imaging," *IEEE Antennas Wireless Propag. Lett.*, vol. 20, no. 6, pp. 1103–1107, Jun. 2021.

[5] D. Ma *et al.*, "Single-shot frequency-diverse near-field imaging using high-scanning-rate leaky-wave antenna," *IEEE Trans. Microw. Theory Techn.*, vol. 69, no. 7, pp. 3399–3412, Jul. 2021.

[6] M. F. Duarte *et al.*, "Single-pixel imaging via compressive sampling," *IEEE Signal Process. Mag.*, vol. 25, no. 2, pp. 83–91, Mar. 2008.

[7] R. I. Stantchev, X. Yu, T. Blu, and E. Pickwell-MacPherson, "Real-time terahertz imaging with a single-pixel detector," *Nature Commun.*, vol. 11, no. 1, pp. 1–8, Dec. 2020.

[8] T. Sleasman, M. F. Imani, J. N. Gollub, and D. R. Smith, "Dynamic metamaterial aperture for microwave imaging," *Appl. Phys. Lett.*, vol. 107, no. 20, Nov. 2015, Art. no. 204104.

[9] O. Yurduseven, D. L. Marks, T. Fromenteze, and D. R. Smith, "Dynamically reconfigurable holographic metasurface aperture for a mills-cross monochromatic microwave camera," *Opt. Exp.*, vol. 26, no. 5, pp. 5281–5291, 2018.

[10] J. Hunt *et al.*, "Metamaterial apertures for computational imaging," *Science*, vol. 339, no. 6117, pp. 310–313, 2013.

[11] T. Fromenteze *et al.*, "Computational imaging using a mode-mixing cavity at microwave frequencies," *Appl. Phys. Lett.*, vol. 106, no. 19, May 2015, Art. no. 194104.

[12] T. Zvolensky, V. R. Gowda, J. Gollub, D. L. Marks, and D. R. Smith, "W-band sparse imaging system using frequency diverse cavity-fed metasurface antennas," *IEEE Access*, vol. 6, pp. 73659–73668, 2018.

[13] T. F. Gallacher, R. Sondena, D. A. Robertson, and G. M. Smith, "Optical modulation of millimeter-wave beams using a semiconductor substrate," *IEEE Trans. Microw Theory Techn.*, vol. 60, no. 7, pp. 2301–2309, Jul. 2012.

[14] T. F. Gallacher, D. A. Robertson, and G. M. Smith, "The photo-injected Fresnel zone plate antenna: Optoelectronic beam steering at mm-wave frequencies," *IEEE Trans. Antennas Propag.*, vol. 61, no. 4, pp. 1688–1696, Apr. 2013.

[15] M. K. Leino, J. Bergman, J. Ala-Laurinaho, and V. Viikari, "Millimeter-wave frequency-diverse imaging with phased array intended for communications," *Prog. Electromagn. Res. M*, vol. 101, pp. 69–78, Feb. 2021.

[16] A. Tamminen, S.-V. Pälli, J. Ala-Laurinaho, A. Aspelin, A. Oinaanoja, and Z. Taylor, "Holograms with neural-network backend for submillimeter-wave beamforming applications," *Proc. SPIE*, vol. 11411, Apr. 2020, Art. no. 114110C.

[17] M. Born and E. Wolf, *Principles of Optics*, 7th ed. Cambridge, U.K.: Cambridge Univ. Press, 1999.

[18] G. Lipworth *et al.*, "Metamaterial apertures for coherent computational imaging on the physical layer," *J. Opt. Soc. Amer. A, Opt. Image Sci.*, vol. 30, no. 8, pp. 1603–1612, 2013.

[19] O. Yurduseven, M. A. B. Abbasi, T. Fromenteze, and V. Fusco, "Lens-loaded coded aperture with increased information capacity for computational microwave imaging," *Remote Sens.*, vol. 12, no. 9, p. 1531, May 2020.

[20] O. Yurduseven *et al.*, "Resolution of the frequency diverse metamaterial aperture imager," *Prog. Electromagn. Res.*, vol. 150, pp. 97–107, Jan. 2015.

[21] G. Barbastathis, A. Ozcan, and G. Situ, "On the use of deep learning for computational imaging," *Optica*, vol. 6, no. 8, pp. 921–943, 2019.

[22] J. Ala-Laurinaho *et al.*, "Measurement of the Odin telescope at 119 GHz with a hologram-type CATR," *IEEE Trans. Antennas Propag.*, vol. 49, no. 9, pp. 1264–1270, Sep. 2001.

[23] T. Koskinen *et al.*, "Experimental study on a hologram-based compact antenna test range at 650 GHz," *IEEE Trans. Microw. Theory Techn.*, vol. 53, no. 9, pp. 2999–3006, Sep. 2005.

[24] J. Salo *et al.*, "Holograms for shaping radio-wave fields," *J. Opt. A, Pure Appl. Opt.*, vol. 4, no. 5, pp. S161–S167, Sep. 2002.

[25] J. Meltaus *et al.*, "Millimeter-wave beam shaping using holograms," *IEEE Trans. Microw. Theory Techn.*, vol. 51, no. 4, pp. 1274–1280, Apr. 2003.

[26] C. A. Balanis, *Advanced Engineering Electromagnetics*, 2nd ed. Hoboken, NJ, USA: Wiley, 2012.

[27] J. A. Kong, *Electromagnetic Wave Theory*. Cambridge, MA, USA: EMW Publishing, 2008.

[28] Q. Fang, P. M. Meaney, and K. D. Paulsen, "Singular value analysis of the Jacobian matrix in microwave image reconstruction," *IEEE Trans. Antennas Propag.*, vol. 54, no. 8, pp. 2371–2380, Aug. 2006.

[29] J. W. Lamb, "Miscellaneous data on materials for millimetre and submillimetre optics," *Int. J. Infr. Millim. Waves*, vol. 17, no. 12, pp. 1997–2034, 1996.

[30] S.-V. Pälli, A. Tamminen, J. Ala-Laurinaho, and Z. Taylor, "Dielectric phase hologram for frequency-diverse millimeter and submillimeter-wave imaging applications," in *Proc. Conf. Lasers Electro-Opt. Eur./Eur. Quantum Electron. Conf. (CLEO/Europe-EQEC)*, 2021, p. 1.

[31] *Keras Documentation*. Accessed: Apr. 7, 2021. [Online]. Available: https://keras.io/

[32] P. F. Goldsmith, *Quasioptical Systems*. London, U.K.: Chapman & Hall, 1998.

[33] S. Zhu *et al.*, "Differential coincidence imaging with frequency diverse aperture," *IEEE Antennas Wireless Propag. Lett.*, vol. 17, no. 6, pp. 964–968, Jun. 2018.

Samu-Ville Pälli was born in Savonlinna, Finland, in 1994. He received the B.Sc. (Tech.) and M.Sc. (Tech.) degrees (Hons.) in electrical engineering from Aalto University, Espoo, Finland, in 2018 and 2020, respectively, where he is currently pursuing the D.Sc. (Tech.) degree.

He has been with the Department of Electronics and Nanoengineering, School of Electrical Engineering, Aalto University, since 2017. His current research interests include computational imaging methods at submillimeter waves and terahertz imaging and sensing.

Aleksi Tamminen (Member, IEEE) was born in Ruotsinpyhtää, Finland, in 1982. He received the B.Sc. (Tech.) and M.Sc. (Tech.) degrees in electrical engineering from Helsinki University of Technology, Espoo, Finland, in 2005 and 2007, respectively, and the Lic.Sc. (Tech.) and D.Sc. (Tech.) degrees from Aalto University (former Helsinki University of Technology), Espoo, in 2011 and 2013, respectively.

From 2005 to 2013, he was with the Department of Radio Science and Engineering, Aalto University. His research work at Aalto University was related to antenna measurements and imaging at millimeter and submillimeter waves. From 2013 to 2018, he was a Research Scientist with Asqella Ltd., Helsinki, Finland. He was a Principal in the research and development of commercial submillimeter-wave imaging technology as well as in participating in academic research projects in the related field. Since 2018, he has been with Aalto University as a Research Fellow. He has authored or coauthored more than 50 scientific journal and conference publications as well as three patent applications. His current research interests are submillimeter- and millimeter-wave projects including antenna measurements, sensing biological tissues, and imaging.

Mr. Tamminen was a recipient of the Young Engineer Prize from the 5th European Radar Conference on November 31, 2008, as well as the Best Student Paper Award from the Global Symposium on Millimeter Waves 2010 on April 14–16, 2010. In addition to research, he served as the organizing secretary of international conference, the 6th ESA Workshop on Millimeter-Wave Technology and Applications, and the 4th Global Symposium on Millimeter Waves, held in Espoo in May 2011.

Juha Ala-Laurinaho received the M.Sc. degree in mathematics and the D.Sc. (Tech.) degree in electrical engineering from TKK Helsinki University of Technology, Espoo, Finland, in 1995 and 2001, respectively.

He has been with TKK, currently Aalto University, Espoo, serving in the Radio Laboratory from 1995 to 2007, with the Department of Radio Science and Engineering from 2008 to 2016. He is currently with the Department of Electronics and Nanoengineering. Currently, he works as a Staff Scientist. He has been a Researcher and the Project Manager in many millimeter-wave technology-related projects. His current research interests are the antennas and antenna measurement techniques for millimeter and submillimeter waves, and millimeter-wave imaging.

Zachary D. Taylor (Member, IEEE) received the B.S. degree in electrical engineering from the University of California (UCLA), Los Angeles, CA, USA, in 2004, and the M.S. and Ph.D. degrees in electrical engineering from the University of California (UCSB), Santa Barbara, CA, in 2006 and 2009, respectively.

From 2013 to 2018, he was an Adjunct Assistant Professor with appointments in the Department of Bioengineering, the Department of Electrical Engineering, and the Department of Surgery, UCLA. Since 2018, he has been an Assistant Professor with the Department of Electronics and Nanoengineering, Aalto University, Espoo, Finland. His current research interests include submillimeter-wave and terahertz imaging, sensing, and calibration.